Improved laser linewidth estimation from self-heterodyne beat note measurements using parametric Wiener filters

Markus Kantner, Lutz Mertenskötter

submitted: December 15, 2022

Weierstrass Institute
Mohrenstr. 39
10117 Berlin
Germany
E-Mail: markus.kantner@wias-berlin.de
          lutz.mertenskoetter@wias-berlin.de

Improved laser linewidth estimation from self-heterodyne beat note measurements using parametric Wiener filters

Markus Kantner, Lutz Mertenskötter

Abstract

Self-heterodyne beat note measurement techniques are widely used for the experimental characterization of the phase noise power spectral density (PSD) and the spectral linewidth of lasers. The measured data, however, must be corrected for the transfer function of the interferometer in a post-processing routine. The standard approach disregards the measurement noise and thereby induces uncontrolled artifacts in the reconstructed noise PSDs. We introduce an improved data post-processing routine based on a parametric Wiener filter (power spectrum equalization, PSE), that is potentially free of reconstruction artifacts provided a good estimate of the signal-to-noise ratio (SNR) is supplied. Based on the PSE filter, we describe a new method for the estimation of the intrinsic laser linewidth. Our method yields accurate estimates even in the case of strong measurement noise, where the intrinsic linewidth plateau is not visible using the standard method. The method is demonstrated for simulated time series data from stochastic laser rate equations.

1   Introduction

Narrow-linewidth lasers exhibiting low phase noise are core elements of coherent optical communication systems [1–3], gravitational wave interferometers [4–7] and emerging quantum technologies, including optical atomic clocks [8–10], matter-wave interferometers [11–13] and ion-trap quantum-computers [14–16]. For many of these applications, the performance depends critically on the laser's intrinsic (Lorentzian) linewidth [17, 18], which is typically obscured by additional $1/f$-like technical noise [19–24]. Because of this so-called *flicker noise*, the laser linewidth alone is not a well-defined quantity and needs to be specified at least together with the measurement time. For a detailed characterization of the phase noise exhibited by the laser (or the fluctuations of its instantaneous frequency), the measurement of the corresponding power spectral density (PSD) is required.

The experimental measurement of the frequency noise power spectral density (FN–PSD) is challenging as the rapid oscillations of the laser's optical field cannot be directly resolved by electronic photodetectors. A standard method that is widely used for the measurement of the FN–PSD is the delayed self-heterodyne (DSH) beat note measurement technique [19, 25–30], which allows to extract the phase fluctuation dynamics from a slow beat note signal in the radio frequency (RF) regime. The evaluation of the method, however, requires some post-processing of the measured data in order to reconstruct the FN–PSD of the free-running laser by removing the footprint of the self-heterodyne interferometer. In this paper we describe an improved post-processing routine based on a parametric Wiener filter (*power spectrum equalization*, PSE) that avoids typical artifacts which occur in the standard method.

This paper is organized as follows: In Sec. 2, we describe the experimental setup and provide a model of the measurement that takes also measurement noise into account. In Sec. 3, we review the Wiener deconvolution method [31] with particular focus on the application to the DSH measurement. Thereby, we discuss a family of frequency-domain filter functions and their capabilities in restoring the true
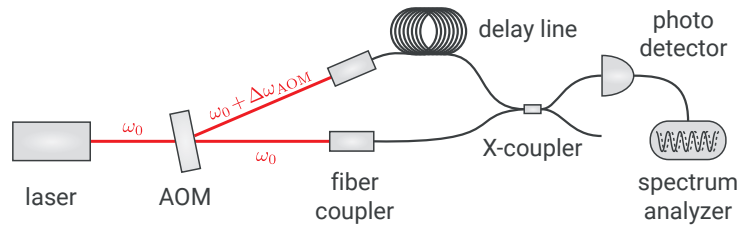
Fig. 1. Illustration of the experimental setup for the DSH beat note measurement. The laser beam is separated by an AOM, where one arm of the signal is frequency shifted and delayed by a long fiber. Both beams are superimposed at a photodetector, which captures only the slow beat note signal in the RF domain.

FN–PSD of the free-running laser. In Sec. 4, we propose a novel method based on the PSE filter, that allows for a precise estimate of the intrinsic linewidth even at low signal-to-noise ratio, when the onset of the intrinsic linewidth plateau is overshadowed by measurement noise. The method is demonstrated for simulated time series of a generic single-mode continuous wave (CW) laser in Sec. 5. We close with a discussion of the method in Sec. 6.

2 Delayed Self-Heterodyne Beat Note Measurement

In the delayed self-heterodyne (DSH) measurement method, see Fig. 1, the light of a laser is superimposed with the frequency-shifted (heterodyne) and time-delayed light from the same source. The frequency shift $\Delta\omega_{\mathrm{AOM}}$ (typically several tens of MHz to $100\,\mathrm{MHz}$) is usually realized with an acousto-optic modulator (AOM) and the delay τ_d is implemented via long (coiled) fibers (typically several km). If the delay is larger than the coherence time of the laser, the delayed light can be regarded as a statistically independent second laser with the same frequency and noise characteristics. The DSH method allows to down-convert the optical signal to a beat note signal in the RF domain, that can be resolved by corresponding spectrum analyzers.

Unlike other methods, the DSH method does not require stabilization of the laser to an optical reference (*e.g.*, a frequency-stabilized second laser, a high-Q optical cavity or an atomic transition). Moreover, the frequency noise characteristics can be measured over a broad frequency bandwidth. A detailed description of the experimental setup and the post-processing procedure can be found in [32].

After down-conversion and I–Q demodulation (Hilbert transform) carried out by the spectrum analyzer, the detected in-phase and quadrature signals read [32]

$$I(t) = \eta_{\mathrm{det}}\sqrt{P(t)\,P(t-\tau_d)}\,\cos\left(\phi(t) - \phi(t-\tau_d) - \Delta\Omega\,t\right) + \xi_I(t), \tag{1a}$$

$$Q(t) = \eta_{\mathrm{det}}\sqrt{P(t)\,P(t-\tau_d)}\,\sin\left(\phi(t) - \phi(t-\tau_d) - \Delta\Omega\,t\right) + \xi_Q(t), \tag{1b}$$

where η_{det} describes the detector efficiency, P is the optical power (or photon number), ϕ is the optical phase and $\Delta\Omega$ is the final difference frequency accumulated in the beating of the signal in the interferometer and the RF analyzer, where the sum frequency components are filtered out. Moreover, we assume Gaussian white measurement noise with correlation function $\langle\xi_I(t)\,\xi_I(t')\rangle = \langle\xi_Q(t)\,\xi_Q(t')\rangle = \sigma_{\mathrm{meas}}^2\delta(t-t')$.

From the detected time series $I(t)$, $Q(t)$ one easily obtains the phase fluctuation difference

$$\Delta\phi(t) = \delta\phi(t) - \delta\phi(t-\tau_d) = \arctan\left(\frac{Q(t)}{I(t)}\right) - \overline{\Omega}\tau_d + \Delta\Omega\,t + \xi_\phi(t) \tag{2}$$

where $\overline{\Omega}$ is the nominal CW frequency and $\delta\phi(t) = \phi(t) - \overline{\Omega}t$. The effective measurement noise $\xi_\phi(t)$ (which derives from $\xi_I(t)$ and $\xi_Q(t)$) is approximately white

$$\langle \xi_\phi(t)\, \xi_\phi(t') \rangle \approx \left(\frac{\sigma_{\mathrm{meas}}}{\eta_{\mathrm{det}}\overline{P}} \right)^2 \delta(t - t'), \tag{3}$$

if the average power $\overline{P}$ is much larger than the measurement noise level σ_{meas}, see Appendix A. The evaluation of (2) requires estimation of τ_d and $\Delta\Omega$ (detrending), see [32] for details.

From the relation between the phase fluctuations of the single laser $\delta\phi(t)$ and $\Delta\phi(t)$, see Eq. (2), which can be written in Fourier space as

$$\Delta\tilde{\phi}(\omega) = H(\omega)\, \delta\tilde{\phi}(\omega), \qquad H(\omega) = 1 - \mathrm{e}^{i\omega\tau_d}, \tag{4}$$

one derives a simple relation between the phase noise PSDs

$$S_{\Delta\phi,\Delta\phi}(\omega) = |H(\omega)|^2\, S_{\delta\phi,\delta\phi}(\omega). \tag{5}$$

In the standard post-processing routine [19, 32], one resolves (5) for $S_{\delta\phi,\delta\phi}(\omega)$ by division through $|H(\omega)|^2 = 2(1 - \cos(\omega\tau_d))$. This approach has two notable shortcomings: First, this procedure does not take into account the measurement noise and thereby over estimates the phase noise PSD at increased measurement noise levels. Second, the transfer function has roots at $\omega_n = 2\pi n/\tau_d$, $n \in \mathbb{Z}$, which turn to poles in its inverse $|G(\omega)|^2 = |H(\omega)|^{-2}$. As a consequence, the reconstructed PSD features a series of equidistant spurious spikes [33–35], resulting from an uncontrolled amplification of the measurement noise.

In principle, the DSH technique also provides access to the relative intensity noise (RIN) PSD, by an analogous post processing routine. This requires, however, a sufficiently long fiber delay exceeding the coherence length of the laser. We refrain from a discussion of the RIN measurement, since our focus in this paper is on the identification of the phase or frequency noise PSD.

3 Parametric Wiener Filter

In this section, we recapitulate Wiener deconvolution [31, 36] as a method for the reconstruction of hidden signals from noisy time series data. Next to the well-known Wiener filter, we present *power spectrum equalization* (PSE) as an important representative of the group of parametric Wiener filters.

Let $x(t)$ denote the time series of a hidden signal of interest that is measured by an experimental setup characterized by a convolution kernel $h(t)$. In the case of the DSH measurement described above, this is $h(t) = \delta(t) - \delta(t - \tau_d)$. Furthermore, let $\xi(t)$ denote additive Gaussian white measurement noise, then the experiment yields an observed time series

$$z(t) = (h * x)(t) + \xi(t). \tag{6a}$$

The process noise and measurement noise are assumed to be uncorrelated $\langle x(t)\, \xi(t') \rangle = 0$. One seeks for an estimate $\hat{x}(t)$ of the hidden signal

$$\hat{x}(t) = (g * z)(t), \tag{6b}$$

cf. Fig. 2, where the (de-)convolution kernel $g(t)$ satisfies an optimality condition.
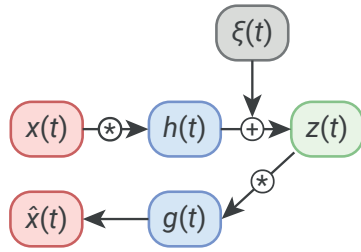
Fig. 2. Schematic illustration of the Wiener deconvolution method (6) for the computation of an optimal reconstruction $\hat{x}(t)$ of a hidden time series $x(t)$ from noisy measurement data $z(t)$.

In this paper, our main interest is the reconstruction of PSDs of hidden signals in the frequency domain, for which we introduce the Fourier space representation of (6)

$$Z(\omega) = H(\omega) X(\omega) + \Xi(\omega), \tag{7a}$$

$$\hat{X}(\omega) = G(\omega) Z(\omega). \tag{7b}$$

From (7b), we obtain the relation between the estimated PSD $S_{\hat{x},\hat{x}}(\omega)$ of the hidden signal and the PSD of the measured time series $S_{z,z}(\omega)$:

$$S_{\hat{x},\hat{x}}(\omega) = |G(\omega)|^2 S_{z,z}(\omega). \tag{8}$$

In the following, we discuss different candidates for the frequency-domain filter function $G(\omega)$. Their performance is evaluated with respect to the reconstruction of the typical FN–PSD of a semiconductor laser [20, 22, 23] from DSH measurements. We take the transfer function of the interferometer as

$$H(\omega) = 1 - e^{i\omega\tau_d}$$

and the hidden signal and noise PSDs

$$S_{x,x}(\omega) = \frac{C}{\omega^\nu} + S_\infty, \tag{9}$$

$$S_{\xi,\xi}(\omega) = \sigma\omega^2. \tag{10}$$

In (9), S_∞ determines the intrinsic laser linewidth, which is obscured by additional colored noise of power-law type with $0.8 \lesssim \nu \lesssim 1.6$ (flicker noise). The functional form (9) is consistent with theoretical models and experimental observations for frequencies well below the relaxation oscillation (RO) peak (typically at several GHz). The level of phase measurement noise, see Eq. (3), is specified by σ and the corresponding frequency measurement noise PSD is a quadratic function of the frequency.[1] The model PSDs (9)–(10) imply the signal-to-noise ratio

$$\mathrm{SNR}(\omega) = \frac{S_{x,x}(\omega)}{S_{\xi,\xi}(\omega)}. \tag{11}$$

Figure 3 shows that different filters $G(\omega)$ can lead to vastly different results for $S_{\hat{x},\hat{x}}(\omega)$. In the following section, we discuss their behavior in more detail.

---

[1]The time-domain relation between phase and frequency fluctuations $\delta\phi(t) = \int^t dt'\, \delta\omega(t')$ implies the following relation in the frequency-domain: $-i\omega\delta\tilde{\phi}(\omega) = \delta\tilde{\omega}(\omega)$. Thus, it holds $S_{\delta\omega,\delta\omega}(\omega) = \omega^2 S_{\delta\phi,\delta\phi}(\omega)$, such that spectrally white phase noise (3) implies a quadratic frequency-dependency of the FN–PSD.
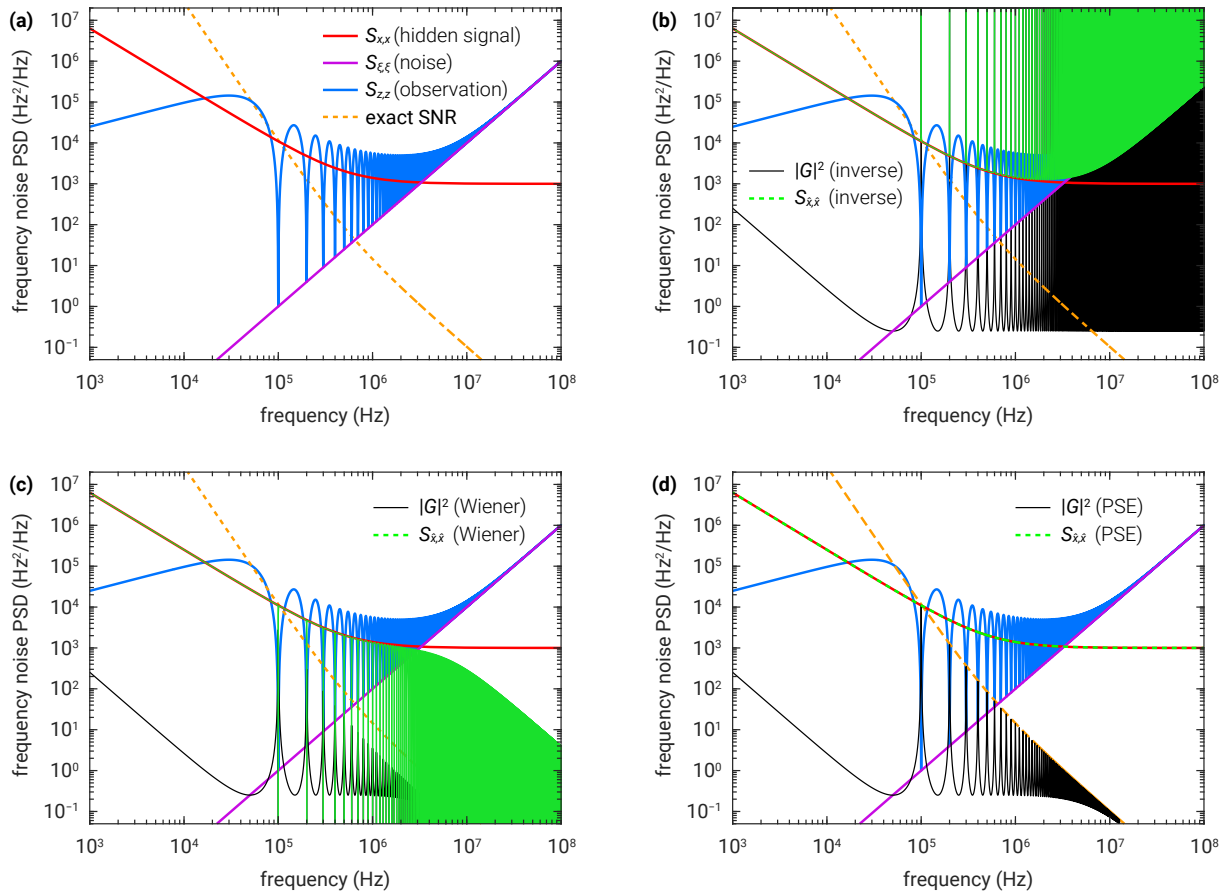
Fig. 3. Comparison of the different filters for PSD reconstruction. **(a)** Analytical signal (9) and measurement noise (10) PSD along with the observed spectrum and the exact signal-to-noise ratio. Parameters in the plot are $\nu = 1.4$, $C = 10^{11}\,\mathrm{Hz}^{\nu+1}$, $S_\infty = 10^3\,\mathrm{Hz}$, $\sigma = 10^{-10}\,\mathrm{Hz}$ and $\tau_d = 10\,\mu\mathrm{s}$. **(b)** The inverse filter (12) yields a reconstructed PSD with spurious artifacts at the poles $f_n = n/\tau_d$, $n \in \mathbb{Z}$, of (12). The intrinsic linewidth plateau is obscured by noise and can not be recovered from the inverse filter reconstruction (merely an upper limit can be extracted). **(c)** The Wiener filter (13) is optimized for time series reconstruction, but fails in reconstruction of the PSD. The reconstructed PSD features sharp dropouts at the pole frequencies and does not follow the hidden signal at low $\mathrm{SNR} < 1$. **(d)** Power spectrum equalization (14) yields an exact reconstruction of the hidden signal's PSD if the exact SNR is provided. Here, the singularities at the poles of the inverse filter are tamed and bounded from above by the SNR, which allows for exact compensation of both the measurement noise and the effects of the interferometer in the observed signal $S_{z,z}$.

3.1 Inverse Filter

In the trivial case of negligible measurement noise, the filter $G(\omega)$ is simply given by the inverse of the transfer function

$$G_{\mathrm{inv}}(\omega) = H^{-1}(\omega). \tag{12}$$

The corresponding estimate of the PSD of the hidden signal reads

$$S_{\hat{x},\hat{x}}(\omega) = |G_{\mathrm{inv}}(\omega)|^2 S_{z,z}(\omega), \qquad |G_{\mathrm{inv}}(\omega)|^2 = \frac{1}{|H(\omega)|^2},$$

which coincides with the standard post-processing method of the DSH measurement [19, 29, 34]. The most prominent feature of the inverse filter $|G_{\mathrm{inv}}(\omega)|^2$ are singularities at poles $\omega_n^{\mathrm{pole}} = 2\pi n/\tau_d$, $n \in \mathbb{Z}$, where the PSD reconstruction fails, see Fig. 3 (a). Sufficiently far away from these poles, the reconstructed spectrum matches the hidden signal as long as the signal-to-noise ratio is large ($\mathrm{SNR} > 1$). If the intrinsic linewidth plateau is obscured by measurement noise, only an upper limit can be extracted via inverse filtering.

3.2 Wiener Filter

Wiener filtering achieves an optimal trade-off between inverse filtering and noise removal. It subtracts the additive noise and reverses the effects of the interferometer simultaneously. The Wiener filter is obtained from minimizing the mean square error of the time-domain signal at an arbitrary instance of time, see Appendix B.1. In the frequency domain, the Wiener filter reads

$$
\begin{aligned}
G_{\mathrm{Wiener}}\left(\omega\right) &= \frac{H^*\left(\omega\right)S_{x,x}\left(\omega\right)}{\left|H\left(\omega\right)\right|^2 S_{x,x}\left(\omega\right)+S_{\xi,\xi}\left(\omega\right)} \\
&= \frac{1}{H\left(\omega\right)}\left(1+\frac{1}{\left|H\left(\omega\right)\right|^2 \mathrm{SNR}\left(\omega\right)}\right)^{-1}
\end{aligned}
\tag{13}
$$

where in the second line we have introduced the signal-to-noise ratio (11).

Although the Wiener filter provides an optimal reconstruction of the time-domain signal, the corresponding PSD reconstruction deviates significantly from the true spectrum in regions of low SNR, see Fig. 3 (c). Moreover, we note that the Wiener filter overemphasizes noise reduction at the poles ω_n^{pole}, where the reconstructed PSD is zero because of

$$
\left|G_{\mathrm{Wiener}}\left(\omega_n^{\mathrm{pole}}\right)\right|^2 = 0
$$

such that also $S_{\hat{x},\hat{x}}\left(\omega_n^{\mathrm{pole}}\right)=0$. Away from these poles and at high SNR, the Wiener filter asymptotically approaches the behavior of the inverse filter

$$
\left|G_{\mathrm{Wiener}}\left(\omega\neq\omega_n^{\mathrm{pole}}\right)\right|^2 \overset{\mathrm{SNR}\to\infty}{\sim} \frac{1}{\left|H\left(\omega\right)\right|^2}.
$$

3.3 Power Spectrum Equalization

Besides the standard Wiener filter, there exist several variants of the method which are collectively referred to as parametric Wiener filters [31]. An important one is *power spectrum equalization* (PSE), which is tailored to minimize the quadratic error of the reconstructed PSD, see Appendix B.2. The corresponding filter function reads

$$
\begin{aligned}
\left|G_{\mathrm{PSE}}\left(\omega\right)\right|^2 &= \frac{S_{x,x}\left(\omega\right)}{\left|H\left(\omega\right)\right|^2 S_{x,x}\left(\omega\right)+S_{\xi,\xi}\left(\omega\right)} \\
&= \frac{1}{\left|H\left(\omega\right)\right|^2}\left(1+\frac{1}{\left|H\left(\omega\right)\right|^2 \mathrm{SNR}\left(\omega\right)}\right)^{-1}.
\end{aligned}
\tag{14}
$$

The PSE filter yields a very accurate reconstruction of the hidden signal when the true frequency-dependent SNR is provided, see Fig. 3 (d).

Most remarkably, the reconstructed spectrum is free of artifacts at the poles of the inverse filter function. This result is easily understood by the following analysis. A straightforward calculation shows that the filter approaches the SNR at ω_n^{pole}

$$
\left|G_{\mathrm{PSE}}\left(\omega_n^{\mathrm{pole}}\right)\right|^2 = \mathrm{SNR}\left(\omega_n^{\mathrm{pole}}\right).
$$

As the interferometer is blind for these frequency components (*i.e.*, the transfer function is zero $H\left(\omega_n^{\mathrm{pole}}\right)=0$), the observed signal contains only measurement noise $S_{z,z}\left(\omega_n^{\mathrm{pole}}\right)=S_{\xi,\xi}\left(\omega_n^{\mathrm{pole}}\right)$,

see Eq. (7b). Finally, substitution into Eq. (8), shows that the PSE filter cancels out the measurement noise exactly and recovers the true signal

$$S_{\hat{x},\hat{x}}\big(\omega_n^{\text{pole}}\big) = \big|G_{\text{PSE}}\big(\omega_n^{\text{pole}}\big)\big|^2 S_{z,z}\big(\omega_n^{\text{pole}}\big)$$
$$= \text{SNR}\big(\omega_n^{\text{pole}}\big) S_{\xi,\xi}\big(\omega_n^{\text{pole}}\big) = S_{x,x}\big(\omega_n^{\text{pole}}\big)$$

if the correct SNR is provided. Furthermore, we observe that the PSE filter restores the hidden signal even in regions of low SNR. This result follows along the same lines as above, starting from $\big|G_{\text{PSE}}(\omega)\big|^2 \overset{\text{SNR}\to 0}{\sim} \text{SNR}(\omega)$. In the opposite case, at very high $\text{SNR}(\omega) \gg 1$, the PSE filter approaches again (just like the Wiener filter) the inverse filter $\big|G_{\text{PSE}}(\omega)\big|^2 \overset{\text{SNR}\to\infty}{\sim} |H(\omega)|^{-2}$.

Finally, we note that all the filter candidates discussed in this section can be written in a unified way as parametric Wiener filters of the following form:

$$\big|G(\omega)\big|^2 = \frac{1}{|H(\omega)|^2}\left(1 + \frac{1}{|H(\omega)|^2\,\text{SNR}(\omega)}\right)^{-m} = \begin{cases} \big|G_{\text{inv}}(\omega)\big|^2 & \text{for } m = 0, \\ \big|G_{\text{Wiener}}(\omega)\big|^2 & \text{for } m = 1, \\ \big|G_{\text{PSE}}(\omega)\big|^2 & \text{for } m = 2. \end{cases}$$

4 Intrinsic Linewidth Estimation at Low Signal-to-Noise Ratio

In the previous section, it was shown that the PSE filter can provide an excellent reconstruction of the hidden PSD if the exact SNR is supplied. At first glance, this approach seems to be rather impractical, since the specification of the exact SNR to a certain extent already anticipates the actual measurement result. One might therefore worry that arbitrary reconstructions could be enforced by the prescribed SNR. It turns out, however, that the PSE filter method exhibits very characteristic artifacts when the specified SNR is incorrect, see Fig. 4. These reconstruction artifacts are easily recognized to be unphysical, such that the incorrect SNR estimate can be rejected. Based on this observation, in the following, we develop a method that simultaneously reconstructs both the PSD of the hidden signal as well as the correct SNR, by minimizing those reconstruction artifacts.

We employ again the analytic model PSDs (9) and (10). For the sake of simplicity, we assume in the following that the parameters C and ν can be accurately estimated from the data, since the low-frequency part of the signal is only negligibly affected by the measurement noise. Similarly, we assume that the noise level σ is known from independent noise floor measurements or from analysis of the RIN signal (which is typically dominated by measurement noise at increased powers). Then, the only free parameter is the intrinsic linewidth value S_∞, that shall be estimated.

Figure 4 (a)–(b) shows the effects of over- and underestimation of S_∞ in the analytical model. Due to the mismatch between the filter function $\big|G_{\text{PSE}}(\omega)\big|^2$ and the observed spectrum $S_{z,z}(\omega)$, spurious oscillations (reconstruction artifacts) show up at frequencies $\omega \approx \omega_n^{\text{pole}}$ in the reconstructed spectrum $S_{\hat{x},\hat{x}}(\omega)$. At large frequencies these oscillations are damped out in both $\big|G_{\text{PSE}}(\omega)\big|^2$ and $S_{z,z}(\omega)$, but their product yields a wrong value of the intrinsic linewidth plateau. We introduce an objective function that penalizes the deviation (*i.e.*, the "inconsistency") between the reconstructed signal $S_{\hat{x},\hat{x}}(\omega; S_\infty)$ (depending on the assumed SNR as a function of estimated S_∞) and the implicitly assumed signal
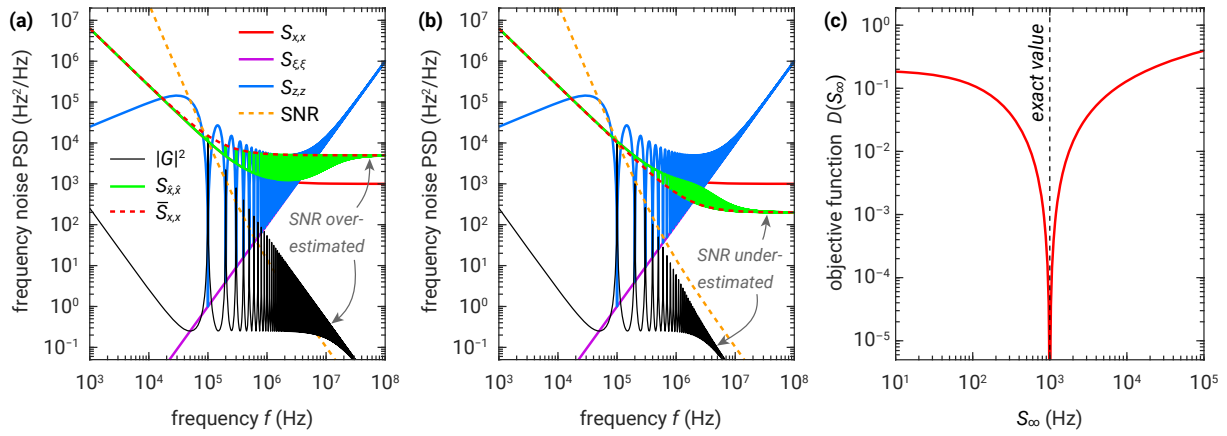
Fig. 4. Reconstruction artifacts in the PSE filter method with incorrectly estimated SNR. **(a)** Overestimation ($S_\infty^{\text{est}} = 5S_\infty$) and **(b)** underestimation ($S_\infty^{\text{est}} = 0.2S_\infty$) of the intrinsic linewidth S_∞ leads to spurious oscillations and spikes in the reconstructed spectrum $S_{\hat{x},\hat{x}}$ (solid red line). In the case of misspecification of the SNR, the maxima of $|G_{\text{PSE}}|^2$ (solid black line) are no longer bounded by the exact SNR (orange dashed line). The assumed $\overline{S}_{x,x}$, which has the functional form (9) and enters the SNR estimate, is shown as red dashed line. The method described in Sec. 4 aims at minimizing the deviation between $\overline{S}_{x,x}$ and $S_{\hat{x},\hat{x}}$ in order to estimate the true value of the intrinsic linewidth parameter S_∞. The corresponding objective function (15) is shown in **(c)**.

$\overline{S}_{x,x}(\omega; S_\infty)$ with the functional form (9) as

$$D\left(S_\infty\right) = \left(\int \mathrm{d}\omega \, \frac{S_{\hat{x},\hat{x}}\left(\omega; S_\infty\right) - \overline{S}_{x,x}\left(\omega; S_\infty\right)}{\overline{S}_{x,x}\left(\omega; S_\infty\right)}\right)^2 \tag{15}$$
$$= \left(\int \mathrm{d}\omega \, \frac{\left|G_{\text{PSE}}\left(\omega; S_\infty\right)\right|^2 S_{z,z}\left(\omega\right) - \overline{S}_{x,x}\left(\omega; S_\infty\right)}{\overline{S}_{x,x}\left(\omega; S_\infty\right)}\right)^2,$$

where the ω–integral runs over a suitable frequency domain. As shown in Fig. 4 (c), the objective function (15) exhibits a sharp minimum at the exact value, cf. Fig. 3 (c). Hence, S_∞ can be estimated by minimization of $D(S_\infty)$.

5 Application to Stochastic Laser Dynamics

In this section, we demonstrate the method described in Sec. 4 for simulated time series data. First, in Sec. 5.1, we describe a stochastic laser rate equation model including non-Markovian colored noise. The latter generates realistic time series including drifts of the instantaneous frequency as commonly observed in semiconductor lasers. In Sec. 5.2, we describe the application of the linewidth estimation method on a sample of DSH measurement data generated from the simulated laser dynamics.

5.1 Stochastic Laser Rate Equations

We consider a single-mode Langevin equation model for the photon number P, the optical phase ϕ and the charge carrier number N

$$\dot{P} = -\gamma\left(P - P_{\text{th}}\right) + \Gamma v_g g\left(P, N\right) P + \Gamma v_g g_{\text{sp}}\left(P, N\right) + F_P, \tag{16a}$$

$$\dot{\phi} = \Omega_0 + \frac{\alpha_H}{2}\Gamma v_g g\left(P, N\right) + F_\phi, \tag{16b}$$

$$\dot{N} = \frac{\eta I}{q} - R\left(N\right) - \Gamma v_g g\left(P, N\right) P - \Gamma v_g g_{\text{sp}}\left(P, N\right) + F_N. \tag{16c}$$
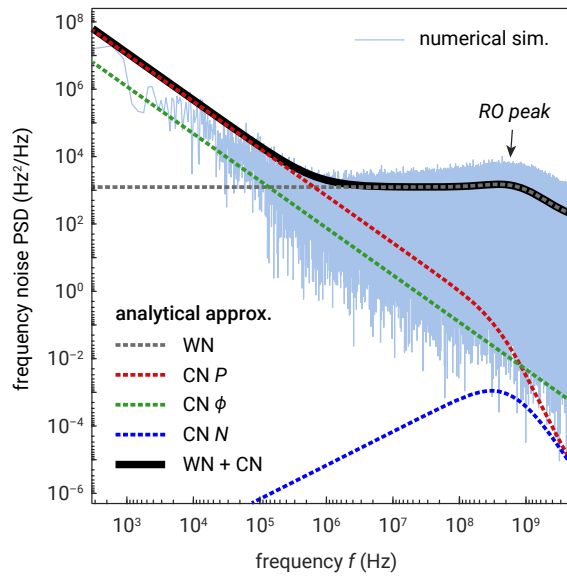
Fig. 5. Numerically computed FN–PSD from simulations of the stochastic laser rate equations (16). Analytical approximations are derived from linearization of the model at the noise-free steady state. White noise (WN) and different colored noise (CN) contributions are indicated separately. Parameters are listed in Tab. 1.

Here, γ is the inverse photon lifetime (due to background absorption and mirror losses), P_{th} is the thermal photon number (Bose–Einstein factor), Γ is the optical confinement factor, v_g is the group velocity, Ω_0 is the detuning from the CW reference frequency, α_H is the linewidth enhancement factor (Henry factor), I is the pump current, η is the injection efficiency and q denotes the elementary charge. The net-gain is modeled as

$$g\left(P, N\right) = \frac{g_0}{1 + \varepsilon P} \log\left(\frac{N}{N_{\text{tr}}}\right), \tag{17}$$

where g_0 is the gain coefficient, N_{tr} is the carrier number at transparency and ε is the gain compression coefficient. Following [18], the spontaneous emission coefficient is described by

$$g_{\text{sp}}\left(P, N\right) = \frac{1}{2} \frac{g_0}{1 + \varepsilon P} \log\left(1 + \left(\frac{N}{N_{\text{tr}}}\right)^2\right), \tag{18}$$

which does not require any additional parameters and is consistent with microscopic gain calculations. Furthermore, (18) avoids the introduction of the population inversion factor [17, 18], that is singular near transparency. The stimulated absorption coefficient is implicitly determined by Eqs. (17)–(18) as $g_{\text{abs}}\left(P, N\right) = g_{\text{sp}}\left(P, N\right) - g\left(P, N\right)$. Non-radiative recombination and spontaneous emission into waste modes are described by

$$R\left(N\right) = AN + \frac{B}{V} N^2 + \frac{C}{V^2} N^3, \tag{19}$$

where A is the Shockley–Read–Hall recombination rate, B is the bimolecular recombination coefficient, C is the Auger recombination coefficient and V is the volume of the active region. All parameter values used in the simulations are listed in Tab. 1.

symbol	description	value
γ	inverse photon lifetime (cavity decay rate)	$5 \cdot 10^{11}\,\mathrm{s}^{-1}$
P_{th}	thermal photon number (Bose–Einstein factor)	$2.7 \cdot 10^{-20}$
Γ	optical confinement factor	0.01
g_0	gain coefficient	$3.54 \cdot 10^{5}\,\mathrm{m}^{-1}$
n_g	group index	3.9
v_g	group velocity, $v_g = n_g/c_0$	$7.69 \cdot 10^{7}\,\mathrm{ms}^{-1}$
N_{tr}	transparency carrier number	$2.5 \cdot 10^{9}$
ε	gain compression coefficient (inverse saturation photon number)	10^{-8}
Ω_0	detuning from CW reference frequency	$0\,\mathrm{Hz}$
α_H	linewidth enhancement factor (Henry factor)	3.0
I	pump current	$200\,\mathrm{mA}$
η	injection efficiency	0.9
A	Shockley–Read–Hall recombination rate	$1 \cdot 10^{8}\,\mathrm{s}^{-1}$
B	bimolecular recombination coefficient	$1 \cdot 10^{16}\,\mathrm{m}^{3}\mathrm{s}^{-1}$
C	Auger recombination coefficient	$4 \cdot 10^{-42}\,\mathrm{m}^{6}\mathrm{s}^{-1}$
V	active region volume	$1.25 \cdot 10^{-15}\,\mathrm{m}^{3}$
ν_P	colored noise exponent (photon number and phase)	1.4
$\sigma_{P,0}$	colored noise amplitude (photon number and phase)	$5 \cdot 10^{5}\,\mathrm{s}^{-(1+\nu_P)/2}$
ν_N	colored noise exponent (carrier number)	1.0
$\sigma_{N,0}$	colored noise amplitude (carrier number)	$10^{9}\,\mathrm{s}^{-(1+\nu_N)/2}$
σ_{meas}	detector noise floor level	$2 \cdot 10^{3}\,\mathrm{s}^{1/2}\,\eta_{\mathrm{det}}$
τ_d	interferometer delay	$10 \cdot 10^{-6}\,\mathrm{s}$

Tab. 1. List of parameter values used in stochastic time series simulation.

The Langevin forces describe zero-mean Gaussian colored noise with the following frequency-domain correlation functions:

$$\langle \tilde{F}_P(\omega) \tilde{F}_P(\omega') \rangle = \left(2\left(\Gamma v_g g_{\mathrm{sp}}\left(\overline{P}, \overline{N}\right) + \gamma P_{\mathrm{th}}\right) \overline{P}\left(1 + \frac{1}{\overline{P}}\right) + \sigma_P^2\left(\overline{P}\right) \frac{1}{\omega^{\nu_P}} \right) \delta\left(\omega - \omega'\right),$$

$$\langle \tilde{F}_\phi(\omega) \tilde{F}_\phi(\omega') \rangle = \left(\left(\Gamma v_g g_{\mathrm{sp}}\left(\overline{P}, \overline{N}\right) + \gamma P_{\mathrm{th}}\right)\left(1 + \frac{1}{\overline{P}}\right) + \left(\frac{\sigma_P\left(\overline{P}\right)}{2\overline{P}}\right)^2 \frac{1}{\omega^{\nu_P}} \right) \delta\left(\omega - \omega'\right),$$

$$\langle \tilde{F}_N(\omega) \tilde{F}_N(\omega') \rangle = \left(2R\left(\overline{N}\right) + 2\Gamma v_g g_{\mathrm{sp}}\left(\overline{P}, \overline{N}\right) \overline{P}\left(1 + \frac{1}{\overline{P}}\right) + \frac{\sigma_N^2\left(\overline{N}\right)}{\omega^{\nu_N}} \right) \delta\left(\omega - \omega'\right), \quad (20)$$

$$\langle \tilde{F}_P(\omega) \tilde{F}_N(\omega') \rangle = -\left(\Gamma v_g g_{\mathrm{sp}}\left(\overline{P}, \overline{N}\right)\left(2\overline{P} + 1\right) - \Gamma v_g g\left(\overline{P}, \overline{N}\right) \overline{P} \right) \delta\left(\omega - \omega'\right),$$

$$\langle \tilde{F}_P(\omega) \tilde{F}_\phi(\omega') \rangle = \langle \tilde{F}_N(\omega) \tilde{F}_\phi(\omega') \rangle = 0.$$

The white noise part of the model features a quantum mechanically correct description of fluctuations due to light-matter interactions [37]. Moreover, we have included three independent $1/f$-type noise sources in (20), with power-law exponents ν_P and ν_N, respectively. The noise amplitudes are taken as $\sigma_P(P) = 2P\sigma_{P,0}$ and $\sigma_N(N) = \sqrt{N}\sigma_{N,0}$ (modeling Hooge's law [38], cf. [39]). The noise correlation functions (20) are formulated at the noise-free steady state $\left(\overline{P}, \overline{N}\right)$. The full nonlinear system of Itô-type stochastic differential equations (SDEs) used for numerical simulation is stated in Appendix C. The numerically simulated FN–PSD is shown in Fig. 5 along with (semi-)analytical approximations from linearization at the noise-free steady state.

5.2   Intrinsic Linewidth Estimation

We apply the method described in Sec. 4 to intrinsic linewidth estimation from simulated DSH measurements. The simulation is carried out in two steps: First, the stochastic laser rate equations (16) are simulated using the Euler–Maruyama method (time step $\Delta t = 50\,\mathrm{ps}$ to resolve the internal laser dynamics) with initial values taken at the noise-free stationary state. In the second step, the DSH measurement is simulated by evaluating (1), which includes addition of Gaussian white measurement noise. The simulated I–Q data are finally used to generate the time series $\Delta\phi$ according to (2). The observed spectrum is computed from $S_{z,z}(\omega) = \omega^2 S_{\Delta\phi,\Delta\phi}(\omega)$ and shown in Fig. 6 (a). For recovery of the original FN–PSD, the PSE filter method is applied to the simulated FN–PSD $S_{z,z}(\omega)$. In the estimation procedure, the frequency domain is restricted to frequencies below the RO peak to ensure validity of the analytical model (9).

The optimal reconstruction of the hidden FN–PSD is shown in Fig. 6 (c) along with corresponding estimates of the SNR and the measurement noise PSD. Evidently, the PSE filter yields a significantly better reconstruction than the inverse filter method, which contains the characteristic reconstruction artifacts and deviates clearly from the hidden signal at increased measurement noise, see Fig. 6 (b). The evaluation of the objective function (15) for the stochastic time series data is shown in Fig. 6 (d). Just like in the case of analytical functions in Sec. 4, the objective function features a sharp minimum near at the exact value.

6   Discussion

The method presented in Sec. 4 not only provides an artifact-free reconstruction of the measured FN–PSD, but also allows to extract the intrinsic linewidth when it is obscured by measurement noise. The procedure, however, relies on the specification of the frequency-dependent SNR in the form of the analytical model (9)–(10). As we have demonstrated in Fig. 4, incorrect SNR estimates lead to reconstruction errors, which are identified as such via inconsistencies with the assumed functional form (9) of the hidden PSD. This *a priori* assumption, however, is well validated both theoretically and experimentally [20, 22, 23], so that no significant bias is to be expected here. Instead, our method exploits this additional prior knowledge about the physics of the problem in order to extract additional information (weak modulations of the measured PSD) from the measurement data which is not used in the inverse filter method.

Even though we restricted the parameter estimation problem in Secs. 4 and 5.2 to a single unknown value (the intrinsic linewidth S_∞), it should be straightforward to extended the method to a multivariate minimization problem where all parameters characterizing the SNR are estimated simultaneously. Furthermore, it would be interesting to apply the estimation method in an analogous way to the reconstruction of the RIN, which is usually much stronger concealed by measurement noise.

In principle also other estimation methods can be employed for reconstruction of the FN–PSD from noisy time series data. For example, Zibar et al. [40] have used an extended Kalman filter to estimate the effect of amplifier noise on the phase noise PSD of a laser. The disadvantage of this method, however, is that it requires a (comprehensive) mathematical model of the dynamical system under measurement, which imposes a significant overhead. Moreover, the application of Kalman filters to problems with large delay (like in the DSH-measurement) where no *ab-initio* estimates of the two-time correlation functions are available, is notoriously difficult and computationally heavy [41, 42]. In contrast, the strength of the PSE filter method is that it is independent of any assumptions on the underlying
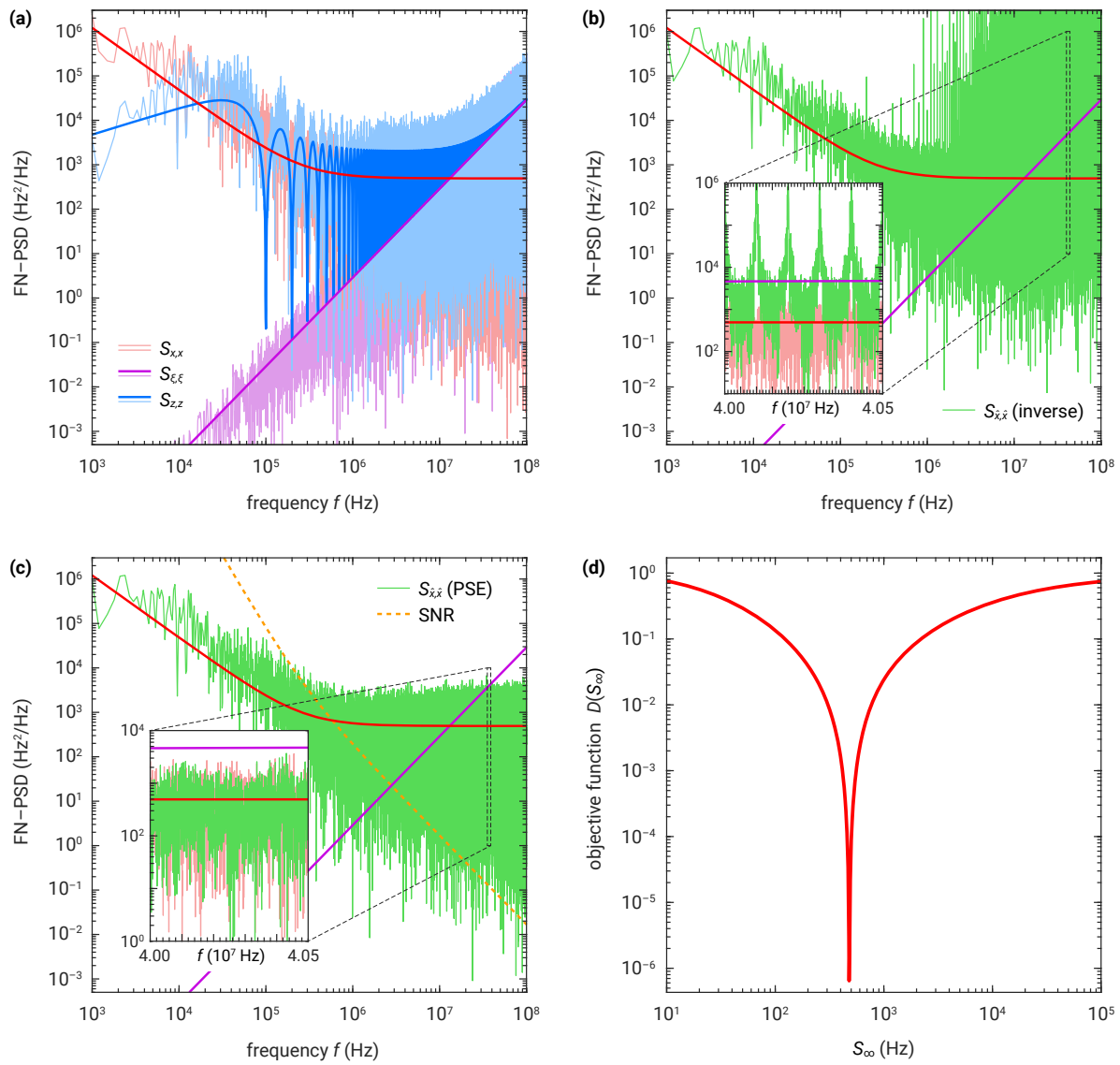
Fig. 6. Application of the linewidth estimation method to simulated time series data. **(a)** PSDs of the hidden signal, the measurement noise and the measured data along with their analytic values. **(b)** Reconstructed PSD using the inverse filter. The inset zooms in on a region with low SNR, where the reconstructed and the true signal deviate by about one order of magnitude. Moreover, we observe reconstruction artifacts around the ω_n^{pole}. **(c)** The PSE filter method yields an accurate reconstruction of the hidden signal even at low SNR that is free of reconstruction artifacts. Here the analytic model PSDs were fitted to the PSD to give the SNR according to the method described in Sec. 4. **(d)** Minimization of the objective function (15) yields an optimal estimate of the intrinsic linewidth parameter at $S_\infty \approx 480\,\mathrm{Hz}$.

state space model. Moreover, since the method is formulated in frequency space, it does not suffer from computational burden due to the large delay. Finally, the method is simple to implement, as it is basically a straightforward extension of the commonly employed inverse filter method (that is still contained as a limiting case).

7 Summary

We have presented an improved post-processing routine for time series data evaluation from DSH linewidth measurements. Our method employs a parametric Wiener filter (power spectrum equalization, PSE) which removes the typical artifacts at the poles of the inverse transfer function commonly

observed in experimental studies [33–35]. We have shown that the PSE filter method enables an accurate estimation of the intrinsic laser linewidth, where the corresponding estimation method is based on the deliberate suppression of the characteristic spurious reconstruction artifacts in the FN–PSD. Remarkably, this allows for the reconstruction of the intrinsic linewidth plateau even when it is obscured by measurement noise. The method has been demonstrated for simulated time series based on a stochastic rate equation model including non-Markovian $1/f$-type noise.

Appendix

A Effective Phase Measurement Noise

We seek for an approximation of the effective phase measurement noise and its two-time correlation function. Starting from (1), we expand for small noise

$$\arctan\left(\frac{Q\left(t\right)}{I\left(t\right)}\right) \approx \arctan\left(\tan\left(\Phi(t)\right) + \frac{\tan\left(\Phi\left(t\right)\right)}{\eta_{\det}\sqrt{P\left(t\right)P\left(t-\tau_d\right)}}\left(\frac{\xi_Q\left(t\right)}{\sin\left(\Phi(t)\right)} - \frac{\xi_I\left(t\right)}{\cos\left(\Phi(t)\right)}\right)\right)$$

where $\Phi\left(t\right) = \phi\left(t\right) - \phi\left(t - \tau_d\right) - \Delta\Omega\, t$. Expansion to first order yields

$$\arctan\left(\frac{Q\left(t\right)}{I\left(t\right)}\right) \approx \Phi\left(t\right) + \frac{1}{\eta_{\det}\sqrt{P\left(t\right)P\left(t-\tau_d\right)}}\left(\cos\left(\Phi\left(t\right)\right)\xi_Q\left(t\right) - \sin\left(\Phi\left(t\right)\right)\xi_I\left(t\right)\right).$$

Expansion at the CW state with $P\left(t\right) = \overline{P} + \delta P\left(t\right)$ and $\phi\left(t\right) = \overline{\Omega}t + \delta\phi\left(t\right)$ yields

$$\Delta\phi\left(t\right) = \delta\phi\left(t\right) - \delta\phi\left(t - \tau_d\right) \approx \arctan\left(\frac{Q\left(t\right)}{I\left(t\right)}\right) - \overline{\Omega}\tau_d + \Delta\Omega\, t + \xi_\phi$$

with the effective phase measurement noise

$$\xi_\phi\left(t\right) = \frac{1}{\eta_{\det}\sqrt{P\left(t\right)P\left(t-\tau_d\right)}}\left(\sin\left(\Phi\left(t\right)\right)\xi_I\left(t\right) - \cos\left(\Phi\left(t\right)\right)\xi_Q\left(t\right)\right).$$

The effective measurement noise clearly has zero mean $\langle\xi_\phi\left(t\right)\rangle = 0$. We approximate the two-time correlation function

$$\begin{aligned}
\langle\xi_\phi\left(t\right)\xi_\phi\left(t'\right)\rangle \approx \frac{1}{\eta_{\det}^2\overline{P}^2}\Big(&\langle\sin\left(\Phi\left(t\right)\right)\sin\left(\Phi\left(t'\right)\right)\rangle\langle\xi_I\left(t\right)\xi_I\left(t'\right)\rangle \\
&- \langle\cos\left(\Phi\left(t\right)\right)\sin\left(\Phi\left(t'\right)\right)\rangle\langle\xi_Q\left(t\right)\xi_I\left(t'\right)\rangle \\
&- \langle\sin\left(\Phi\left(t\right)\right)\cos\left(\Phi\left(t'\right)\right)\rangle\langle\xi_I\left(t\right)\xi_Q\left(t'\right)\rangle \\
&+ \langle\cos\left(\Phi\left(t\right)\right)\cos\left(\Phi\left(t'\right)\right)\rangle\langle\xi_Q\left(t\right)\xi_Q\left(t'\right)\rangle\Big),
\end{aligned}$$

where we have neglected photon number fluctuations and factorized the phase and measurement fluctuations. Using $\langle\xi_I\left(t\right)\xi_I\left(t'\right)\rangle = \langle\xi_Q\left(t\right)\xi_Q\left(t'\right)\rangle = \sigma_{\mathrm{meas}}^2\delta\left(t-t'\right)$ and stationarity $\langle\xi_I\left(t\right)\xi_Q\left(t'\right)\rangle = \langle\xi_I\left(t'\right)\xi_Q\left(t\right)\rangle$, we arrive at

$$\langle\xi_\phi\left(t\right)\xi_\phi\left(t'\right)\rangle \approx \frac{1}{\eta_{\det}^2\overline{P}^2}\left(\sigma_{\mathrm{meas}}^2\delta\left(t-t'\right) - \langle\sin\left(\Phi\left(t\right) + \Phi\left(t'\right)\right)\rangle\langle\xi_I\left(t'\right)\xi_Q\left(t\right)\rangle\right).$$

The rapidly oscillating cross-correlation term can be neglected such that the effective correlation function is given by Eq. (3).

B   Derivation of the Frequency Domain Filter Functions

In the following, we derive the expressions (13) and (14) using calculus of variations.

B.1   Wiener Filter

We consider the mean square error between the hidden signal $x\left(t\right)$ and its reconstruction (6b) at an arbitrary instance of time t

$$E\left(t\right) = \left\langle \left(\hat{x}\left(t\right) - x\left(t\right)\right)^2 \right\rangle.$$

Fourier transform and substitution of (7) yields

$$E\left(t\right) = \int_{-\infty}^{\infty} \frac{\mathrm{d}\omega}{2\pi} \int_{-\infty}^{\infty} \frac{\mathrm{d}\omega'}{2\pi} \, \mathrm{e}^{-i(\omega-\omega')t} \Bigg(\left[G^*\left(\omega'\right) H^*\left(\omega'\right) - 1\right]\left[G\left(\omega\right) H\left(\omega\right) - 1\right] \left\langle X(\omega)X^*(\omega')\right\rangle$$

$$+ 2\mathrm{Re}\left(G^*\left(\omega'\right)\left[G\left(\omega\right) H\left(\omega\right) - 1\right]\left\langle X\left(\omega\right) \Xi^*\left(\omega'\right)\right\rangle\right) + G^*\left(\omega'\right) G\left(\omega\right)\left\langle \Xi\left(\omega\right) \Xi^*\left(\omega'\right)\right\rangle \Bigg).$$

Next we substitute the expressions for the signal and noise PSDs

$$\frac{1}{2\pi}\left\langle X\left(\omega\right) X^*\left(\omega'\right)\right\rangle = S_{x,x}\left(\omega\right) \delta\left(\omega - \omega'\right), \qquad \frac{1}{2\pi}\left\langle \Xi\left(\omega\right) \Xi^*\left(\omega'\right)\right\rangle = S_{\xi,\xi}\left(\omega\right) \delta\left(\omega - \omega'\right),$$

and assume that the process and measurement noise are uncorrelated $\left\langle X\left(\omega\right) \Xi^*\left(\omega'\right)\right\rangle = 0$. This leads to

$$E\left(t\right) = \int_{-\infty}^{\infty} \frac{\mathrm{d}\omega}{2\pi} \left(\left|G\left(\omega\right) H\left(\omega\right) - 1\right|^2 S_{x,x}\left(\omega\right) + \left|G\left(\omega\right)\right|^2 S_{\xi,\xi}\left(\omega\right) \right),$$

which is entirely independent of the time t. Minimization of the reconstruction error $E\left(t\right)$ is achieved by taking the Gâteaux derivative with respect to $G\left(\omega\right) \to G\left(\omega\right) + \varepsilon\delta G\left(\omega\right)$

$$0 \stackrel{!}{=} \lim_{\varepsilon \to 0} \frac{E\left[G + \varepsilon\delta G\right] - E\left[G\right]}{\varepsilon} = \int_{-\infty}^{\infty} \frac{\mathrm{d}\omega}{2\pi} \Bigg(\left(G\left(\omega\right) H\left(\omega\right) - 1\right) H^*\left(\omega\right) S_{x,x}\left(\omega\right)$$

$$+ G\left(\omega\right) S_{\xi,\xi}\left(\omega\right) \Bigg)\delta G^*\left(\omega\right) + \mathrm{c.c.}$$

where the variation $\delta G\left(\omega\right)$ is arbitrary. From this, we extract the expression for the Wiener filter (13).

B.2   Power Spectrum Equalization

We seek for an optimal reconstruction $S_{\hat{x},\hat{x}}\left(\omega\right)$ of the PSD that minimizes the quadratic error

$$E = \int_{-\infty}^{\infty} \mathrm{d}\omega \left(S_{\hat{x},\hat{x}}\left(\omega\right) - S_{x,x}\left(\omega\right)\right)^2.$$

Starting from the definition of the reconstructed PSD

$$S_{\hat{x},\hat{x}}\left(\omega\right) \delta\left(\omega - \omega'\right) = \frac{1}{2\pi}\langle \hat{X}\left(\omega\right) \hat{X}^*\left(\omega'\right)\rangle,$$

we substitute Eq. (7) and the assume vanishing correlation between process and measurement noise $\langle X(\omega)\,\Xi^*(\omega')\rangle = 0$. With this, we arrive at

$$S_{\hat{x},\hat{x}}(\omega)\,\delta(\omega-\omega') = |G(\omega)|^2 \left(|H(\omega)|^2\,S_{x,x}(\omega) + S_{\xi,\xi}(\omega)\right)\delta(\omega-\omega')\,.$$

The last line allows to rewrite the expression for the reconstruction error as

$$E = \int_{-\infty}^{\infty} \mathrm{d}\omega \,\left(\left(|G(\omega)\,H(\omega)|^2 - 1\right)S_{x,x}(\omega) + |G(\omega)|^2\,S_{\xi,\xi}(\omega)\right)^2\,.$$

Minimization of the error by variation of the filter $G(\omega) \to G(\omega) + \varepsilon\delta G(\omega)$ yields

$$0 \overset{!}{=} \lim_{\varepsilon\to 0} \frac{E[G+\varepsilon\delta G] - E[G]}{\varepsilon} = 2\int_{-\infty}^{\infty}\mathrm{d}\omega\,\left(|H(\omega)|^2\,S_{x,x}(\omega) + S_{\xi,\xi}(\omega)\right)\times$$
$$\times\left(\left(|G(\omega)\,H(\omega)|^2 - 1\right)S_{x,x}(\omega) + |G(\omega)|^2\,S_{\xi,\xi}(\omega)\right)$$
$$\times\left(G(\omega)\,\delta G^*(\omega) + G^*(\omega)\,\delta G(\omega)\right),$$

from which we find (14) to be the optimal filter.

C Itô-Type Stochastic Differential Equations

The Langevin equations (16) can be written as a system of Itô-type stochastic differential equations

$$\mathrm{d}P = \left(-\gamma(P-P_{\mathrm{th}}) + \Gamma v_g g(P,N)P + \Gamma v_g g_{\mathrm{sp}}(P,N) + \sigma_P(P)\mathcal{F}_P\right)\mathrm{d}t \tag{21a}$$
$$+ \sqrt{\gamma(1+P_{\mathrm{th}})P}\,\mathrm{d}W_{\mathrm{out}}^P + \sqrt{\gamma P_{\mathrm{th}}(1+P)}\,\mathrm{d}W_{\mathrm{in}}^P + \sqrt{\Gamma v_g g_{\mathrm{sp}}(P,N)P}\,\mathrm{d}W_{\mathrm{st-em}}^P$$
$$+ \sqrt{\Gamma v_g g_{\mathrm{abs}}(P,N)P}\,\mathrm{d}W_{\mathrm{st-abs}}^P + \sqrt{\Gamma v_g g_{\mathrm{sp}}(P,N)}\,\mathrm{d}W_{\mathrm{sp}}^P,$$
$$\mathrm{d}\phi = \left(\Omega_0 + \frac{\alpha_H}{2}\Gamma v_g g(P,N) + \frac{\sigma_P(P)}{2P}\mathcal{F}_\phi\right)\mathrm{d}t \tag{21b}$$
$$+ \frac{1}{2P}\left(\sqrt{\gamma(1+P_{\mathrm{th}})P}\,\mathrm{d}W_{\mathrm{out}}^\phi + \sqrt{\gamma P_{\mathrm{th}}(1+P)}\,\mathrm{d}W_{\mathrm{in}}^\phi + \sqrt{\Gamma v_g g_{\mathrm{sp}}(P,N)P}\,\mathrm{d}W_{\mathrm{st-em}}^\phi\right.$$
$$\left.+ \sqrt{\Gamma v_g g_{\mathrm{abs}}(P,N)P}\,\mathrm{d}W_{\mathrm{st-abs}}^\phi + \sqrt{\Gamma v_g g_{\mathrm{sp}}(P,N)}\,\mathrm{d}W_{\mathrm{sp}}^\phi\right),$$
$$\mathrm{d}N = \left(\frac{\eta I}{q} - R(N) - \Gamma v_g g(P,N)P - \Gamma v_g g_{\mathrm{sp}}(P,N) + \sigma_N(N)\mathcal{F}_N\right)\mathrm{d}t \tag{21c}$$
$$+ \sqrt{\frac{\eta I}{q}}\,\mathrm{d}W_I + \sqrt{R(N)}\,\mathrm{d}W_R - \sqrt{\Gamma v_g g_{\mathrm{sp}}(P,N)P}\,\mathrm{d}W_{\mathrm{st-em}}^P$$
$$- \sqrt{\Gamma v_g g_{\mathrm{abs}}(P,N)P}\,\mathrm{d}W_{\mathrm{st-abs}}^P - \sqrt{\Gamma v_g g_{\mathrm{sp}}(P,N)}\,\mathrm{d}W_{\mathrm{sp}}^P.$$

Here, $\mathrm{d}W \sim \mathrm{Normal}(0,\mathrm{d}t)$ denotes the increment of the standard Wiener processes (Gaussian white noise) [43]. Wiener processes with different sub- and superscripts are statistically independent. Construction of the colored noise sources $\mathcal{F}_{P,\phi,N}$ is described in Appendix D.

D   Colored Noise

Colored noise sources $\mathcal{F}_{P,\phi,N}$ (the subscripts are omitted in the following) are modeled in the standard way [44] as a *Markovian embedding* via superposition of independent Ornstein–Uhlenbeck (OU) fluctuators

$$\mathcal{F}\left(t\right) = \sqrt{A}\frac{1}{\sqrt{n}}\sum_{i=1}^{n}X_i\left(t\right)$$

where

$$\mathrm{d}X_i\left(t\right) = -\gamma_i X_i\left(t\right)\,\mathrm{d}t + \sqrt{2\gamma_i}\,\mathrm{d}W_i\left(t\right).$$

Here, n is the number of OU fluctuators and A is a normalization constant (see below). The fluctuators are statistically independent, *i.e.*, $\mathrm{d}W_i\left(t\right)\mathrm{d}W_j\left(t\right) = \delta_{i,j}\mathrm{d}t$. From the stationary covariance

$$C_{X_i,X_j}\left(\tau\right) = \langle X_i\left(t+\tau\right)X_j\left(t\right)\rangle = \delta_{i,j}\,\mathrm{e}^{-\gamma_i|\tau|},$$

we obtain the auto-correlation function of the colored noise

$$C_{\mathcal{F},F}\left(\tau\right) = \frac{A}{n}\sum_{j=1}^{n}\mathrm{e}^{-\gamma_j|\tau|}.$$

The corresponding PSD is obtained according to the Wiener–Khinchin theorem [45] by Fourier transform

$$S_{\mathcal{F},\mathcal{F}}\left(\omega\right) = \int_{-\infty}^{\infty}\mathrm{d}\tau\,\mathrm{e}^{i\omega\tau}C_{F,F}\left(\tau\right) = A\frac{1}{N}\sum_{j=1}^{N}\frac{2\gamma_j}{\omega^2+\gamma_j^2}$$

$$= A\int_0^{\infty}\mathrm{d}\gamma\,\rho\left(\gamma\right)\frac{2\gamma}{\omega^2+\gamma^2},$$

where we introduced the continuous distribution of the relaxation rates

$$\rho\left(\gamma\right) = \frac{1}{n}\sum_{j=1}^{n}\delta\left(\gamma-\gamma_j\right). \tag{22}$$

In the following, we consider a power-law distribution

$$\rho\left(\gamma\right) = \frac{C_\nu}{\gamma^\nu}\Theta\left(\gamma-\gamma_0\right)\Theta\left(\gamma_\infty-\gamma\right),\qquad 0 < \nu < 2, \tag{23}$$

with lower and upper cutoffs denoted as γ_0 and γ_∞. The normalization constant $C_\nu = \left(1-\nu\right)/\left(\gamma_\infty^{1-\nu}-\gamma_0^{1-\nu}\right)$ ensures normalization $\int_0^\infty\mathrm{d}\gamma\,\rho\left(\gamma\right) = 1$. From (23), we find that

$$S_{\mathcal{F},\mathcal{F}}\left(\omega\right) = 2AC_\nu\int_{\gamma_0}^{\gamma_\infty}\mathrm{d}\gamma\,\frac{\gamma^{1-\nu}}{\omega^2+\gamma^2} = \frac{2AC_\nu}{\omega^\nu}\int_{\gamma_0/\omega}^{\gamma_\infty/\omega}\mathrm{d}x\,\frac{x^{1-\nu}}{1+x^2}.$$

The integral can formally be solved by a hypergeometric function. More insight, however, is obtained from consideration of the asymptotic limit $\gamma_0 \to 0$ and $\gamma_\infty \to \infty$, which leads to

$$\int_0^\infty\mathrm{d}x\,\frac{x^{1-\nu}}{1+x^2} = \frac{\pi}{2}\frac{1}{\sin\left(\frac{\pi\nu}{2}\right)}.$$

Hence, the PSD exhibits a power-law type frequency-dependency in an arbitrary large frequency window $\gamma_\infty^{-1} \ll \omega \ll \gamma_0^{-1}$

$$S_{\mathcal{F},\mathcal{F}}\left(\gamma_\infty^{-1} \ll \omega \ll \gamma_0^{-1}\right) \sim \frac{1}{\omega^\nu}\frac{AC_\nu\pi}{\sin\left(\frac{\pi\nu}{2}\right)}.$$

Finally, the normalization constant A is chosen as

$$A = \frac{\sin\left(\frac{\pi\nu}{2}\right)}{C_\nu\pi}$$

in order to enforce

$$S_{\mathcal{F},\mathcal{F}}\left(\gamma_\infty^{-1} \ll \omega \ll \gamma_0^{-1}\right) \approx \frac{1}{\omega^\nu},$$

cf. Eq. (20). For the practical generation of time series with the desired scaling of the corresponding PSD, it is necessary to approximate the corresponding distribution function (23) of the relaxation rates by finitely many γ_i. The optimal choice of the n relaxation rates is obtained by inverse transform sampling using the cumulative distribution function of Eq. (23) and a uniform grid on $[0,1]$.

References

[1] K. Kikuchi, "Fundamentals of coherent optical fiber communications", J. Lightwave Technol. **34**, 157–179 (2016) DOI: 10.1109/JLT.2015.2463719.

[2] K. Zhou, Q. Zhao, X. Huang, C. Yang, C. Li, E. Zhou, X. Xu, K. K. Wong, H. Cheng, J. Gan, Z. Feng, M. Peng, Z. Yang, and S. Xu, "kHz-order linewidth controllable 1550 nm single-frequency fiber laser for coherent optical communication", Opt. Express **25**, 19752 (2017) DOI: 10.1364/OE.25.019752.

[3] H. Guan, A. Novack, T. Galfsky, Y. Ma, S. Fathololoumi, A. Horth, T. N. Huynh, J. Roman, R. Shi, M. Caverley, Y. Liu, T. Baehr-Jones, K. Bergman, and M. Hochberg, "Widely-tunable, narrow-linewidth III-v/silicon hybrid external-cavity laser for coherent communication", Opt. Express **26**, 7920 (2018) DOI: 10.1364/OE.26.007920.

[4] B Willke, K Danzmann, M Frede, P King, D Kracht, P Kwee, O Puncken, R. L. Savage, B Schulz, F Seifert, C Veltkamp, S Wagner, P Weßels, and L Winkelmann, "Stabilized lasers for advanced gravitational wave detectors", Class. Quantum Grav. **25**, 114040 (2008) DOI: 10.1088/0264-9381/25/11/114040.

[5] B. P. Abbott et al., "LIGO: the laser interferometer gravitational-wave observatory", Rep. Prog. Phys. **72**, 076901 (2009) DOI: 10.1088/0034-4885/72/7/076901.

[6] K. Dahl, P. Cebeci, O. Fitzau, M. Giesberts, C. Greve, M. Krutzik, A. Peters, S. A. Pyka, J. Sanjuan, M. Schiemangk, T. Schuldt, K. Voss, and A. Wicht, "A new laser technology for LISA", in International conference on space optics (icso 2018), edited by N. Karafolas, Z. Sodnik, and B. Cugny (2019), p. 111800C, DOI: 10.1117/12.2535931.

[7] D. Kapasi, J Eichholz, T McRae, R. Ward, B. Slagmolen, S Legge, K. Hardman, P. Altin, and D. McClelland, "Tunable narrow-linewidth laser at 2 μm wavelength for gravitational wave detector research", Optics Express **28**, 3280–3288 (2020) DOI: 10.1364/oe.383685.

[8] J. Camparo, "The rubidium atomic clock and basic research", Phys. Today **60**, 33–39 (2007) DOI: 10.1063/1.2812121.

[9] A. D. Ludlow, M. M. Boyd, J. Ye, E. Peik, and P. O. Schmidt, "Optical atomic clocks", Rev. Modern Phys. **87**, 637–701 (2015) DOI: 10.1103/RevModPhys.87.637.

[10] Z. L. Newman, V. Maurice, C. Fredrick, T. Fortier, H. Leopardi, L. Hollberg, S. A. Diddams, J. Kitching, and M. T. Hummon, "High-performance, compact optical standard", Opt. Lett. **46**, 4702 (2021) DOI: 10.1364/OL.435603.

[11] A Peters, K. Y. Chung, and S Chu, "High-precision gravity measurements using atom interferometry", Metrologia **38**, 25–61 (2001) DOI: 10.1088/0026-1394/38/1/4.

[12] P. Cheinet, B. Canuel, F. P. D. Santos, A. Gauguet, F. Yver-Leduc, and A. Landragin, "Measurement of the sensitivity function in a time-domain atomic interferometer", IEEE Trans. Instrum. Meas. **57**, 1141–1148 (2008) DOI: 10.1109/TIM.2007.915148.

[13] O. Carraz, F. Lienhart, R. Charrière, M. Cadoret, N. Zahzam, Y. Bidel, and A. Bresson, "Compact and robust laser system for onboard atom interferometry", Appl. Phys. B **97**, 405–411 (2009) DOI: 10.1007/s00340-009-3675-9.

[14] N. Akerman, N. Navon, S. Kotler, Y. Glickman, and R. Ozeri, "Universal gate-set for trapped-ion qubits using a narrow linewidth diode laser", New. J. Phys. **17**, 113060 (2015) DOI: 10.1088/1367-2630/17/11/113060.

[15] C. D. Bruzewicz, J. Chiaverini, R. McConnell, and J. M. Sage, "Trapped-ion quantum computing: progress and challenges", Appl. Phys. Rev. **6**, 021314 (2019) DOI: 10.1063/1.5088164.

[16] I. Pogorelov et al., "Compact ion-trap quantum computing demonstrator", PRX Quantum **2**, 020343 (2021) DOI: 10.1103/PRXQuantum.2.020343.

[17] C. Henry, "Phase noise in semiconductor lasers", J. Lightwave Technol. **4**, 298–311 (1986) DOI: 10.1109/JLT.1986.1074721.

[18] H. Wenzel, M. Kantner, M. Radziunas, and U. Bandelow, "Semiconductor laser linewidth theory revisited", Appl. Sci. **11**, 6004 (2021) DOI: 10.3390/app11136004.

[19] K. Kikuchi and T. Okoshi, "Dependence of semiconductor laser linewidth on measurement time: evidence of predominance of 1/f noise", Electron. Lett. **21**, 1011 (1985) DOI: 10.1049/el:19850717.

[20] K. Kikuchi, "Effect of 1/f-type FM noise on semiconductor-laser linewidth residual in high-power limit", IEEE J. Quant. Electron. **25**, 684–688 (1989) DOI: 10.1109/3.17331.

[21] L. B. Mercer, "1/f frequency noise effects on self-heterodyne linewidth measurements", J. Lightwave Technol. **9**, 485–493 (1991) DOI: 10.1109/50.76663.

[22] Y. Salvadé and R. Dändliker, "Limitations of interferometry due to the flicker noise of laser diodes", J. Opt. Soc. Amer. A **17**, 927–932 (2000) DOI: 10.1364/JOSAA.17.000927.

[23] G. M. Stéphan, T. T. Tam, S. Blin, P. Besnard, and M. Têtu, "Laser line shape and spectral density of frequency noise", Phys. Rev. A **71**, 043809 (2005) DOI: 10.1103/PhysRevA.71.043809.

[24] S. Spießberger, M. Schiemangk, A. Wicht, H. Wenzel, G. Erbert, and G. Tränkle, "DBR laser diodes emitting near 1064 nm with a narrow intrinsic linewidth of 2 kHz", Appl. Phys. B **104**, 813–818 (2011) DOI: 10.1007/s00340-011-4644-7.

[25] T. Okoshi, K. Kikuchi, and A. Nakayama, "Novel method for high resolution measurement of laser output spectrum", Electron. Lett. **16**, 630 (1980) DOI: 10.1049/el:19800437.

[26] J. Dawson, N. Park, and K. Vahala, "An improved delayed self-heterodyne interferometer for linewidth measurements", IEEE Photonics Technology Letters **4**, 1063–1066 (1992) DOI: 10.1109/68.157150.

[27] P. Horak and W. H. Loh, "On the delayed self-heterodyne interferometric technique for determining the linewidth of fiber lasers", Opt. Express **14**, 3923 (2006) DOI: 10.1364/oe.14.003923.

[28] H. Tsuchida, "Laser frequency modulation noise measurement by recirculating delayed self-heterodyne method", Optics Letters **36**, 681 (2011) DOI: 10.1364/OL.36.000681.

[29] M. Schiemangk, S. Spießberger, A. Wicht, G. Erbert, G. Tränkle, and A. Peters, "Accurate frequency noise measurement of free-running lasers", Appl. Optics **53**, 7138 (2014) DOI: 10.1364/AO.53.007138.

[30] Z. Bai, Z. Zhao, Y. Qi, J. Ding, S. Li, X. Yan, Y. Wang, and Z. Lu, "Narrow-linewidth laser linewidth measurement technology", Front. Phys. **9**, DOI: 10.3389/fphy.2021.768165 (2021) DOI: 10.3389/fphy.2021.768165.

[31] J. S. Lim, *Two-dimensional signal and image processing* (Prentice Hall, 1990).

[32] M. Schiemangk, "Ein Lasersystem für Experimente mit Quantengasen unter Schwerelosigkeit", PhD thesis (Humboldt University Berlin, 2019), DOI: 10.18452/19826.

[33] W. Lewoczko-Adamczyk, C. Pyrlik, J. Häger, S. Schwertfeger, A. Wicht, A. Peters, G. Erbert, and G. Tränkle, "Ultra-narrow linewidth DFB-laser with optical feedback from a monolithic confocal Fabry–Perot cavity", Opt. Express **23**, 9705–9709 (2015) DOI: 10.1364/oe.23.009705.

[34] S. Wenzel, O. Brox, P. D. Casa, H. Wenzel, B. Arar, S. Kreutzmann, M. Weyers, A. Knigge, A. Wicht, and G. Tränkle, "Monolithically integrated extended cavity diode laser with 32 kHz 3 dB linewidth emitting at 1064 nm", Laser Photonics Rev., 2200442 (2022) DOI: 10.1002/lpor.202200442.

[35] R. R. Kumar, A. Hänsel, M. F. Brusatori, L. Nielsen, L. M. Augustin, N. Volet, and M. J. R. Heck, "A 10-kHz intrinsic linewidth coupled extended-cavity DBR laser monolithically integrated on an InP platform", Opt. Lett. **47**, 2346 (2022) DOI: 10.1364/OL.454478.

[36] A. T. Walden, "Robust deconvolution by modified wiener filtering", Geophysics **53**, 186–191 (1988) DOI: 10.1190/1.1442453.

[37] L. A. Coldren, S. W. Corzine, and M. L. Mašanović, *Diode lasers and photonic integrated circuits* (Wiley, Hoboken (NJ), 2012), DOI: 10.1002/9781118148167.

[38] F. N. Hooge, "1/f noise sources", IEEE Transactions on Electron Devices **41**, 1926–1935 (1994) DOI: 10.1109/16.333808.

[39] I. A. Garmash, M. V. Zverkov, N. B. Kornilova, V. N. Morozov, R. F. Nabiev, A. T. Semenov, M. A. Sumarokov, and V. R. Shidlovskii, "Analysis of low-frequency fluctuation of the radiation power of injection lasers", J. Sov. Laser Res. **10**, 459–476 (1989) DOI: 10.1007/BF01442220.

[40]   D. Zibar, J. E. Pedersen, P. Varming, G. Brajato, and F. D. Ros, "Approaching optimum phase measurement in the presence of amplifier noise", Optica **8**, 1262 (2021) DOI: 10.1364/OPTICA.431668.

[41]   H. L. Alexander, "State estimation for distributed systems with sensing delay", SPIE Proc. Data Stuctures and Target Classification **1470**, edited by V. Libby, 103–111 (1991) DOI: 10.1117/12.44843.

[42]   A. Gopalakrishnan, N. S. Kaisare, and S. Narasimhan, "Incorporating delayed and infrequent measurements in extended Kalman filter based nonlinear state estimation", J. Process Control **21**, 119–129 (2011) DOI: 10.1016/j.jprocont.2010.10.013.

[43]   K. Jacobs, *Stochastic processes for physicists* (Cambridge University Press, Cambridge, 2010), DOI: 10.1017/CBO9780511815980.

[44]   S. M. Kogan, *Electronic noise and fluctuations in solids* (Cambridge University Press, Cambridge, 1996), DOI: 10.1017/CBO9780511551666.

[45]   R. Kubo, M. Toda, and N. Hashitsume, *Statistical physics II: nonequilibrium statistical mechanics*, 2nd, Vol. 31, Springer Series in Solid-State Sciences (Springer, Berlin, Heidelberg, 1991), DOI: 10.1007/978-3-642-58244-8.